

**Finding Fault in Dyer County, Tennessee: Exploring the Relationships of Earthquake-Induced
Liquefaction Features to Subsurface Faults**

by

John Johnson

A thesis submitted to the Graduate Faculty of
Auburn University
in partial fulfillment of the
requirements for the Degree of
Master of Science

Auburn, Alabama
December 15, 2018

Copyright 2018 by John Johnson

Approved by
Lorraine W. Wolf, Chair, Professor of Geosciences
Mark G. Steltenpohl, Professor of Geosciences
Stephanie Shepherd, Professor of Geosciences

Abstract

The New Madrid Seismic Zone (NMSZ) is located within the northern Mississippi Embayment, a northeast-striking graben that formed as a part of a failed rift system and later filled with sediments. Although this intracontinental region exhibits mostly low-magnitude seismicity today, the region experienced three large earthquake sequences ($M > 7$) in 1811-1812. Seismic sources of the seismicity in the NMSZ are recognized by patterns of earthquake epicenters; however, surface evidence of these structures is lacking. This study is aimed at identifying seismogenic faults responsible for the earthquake-induced liquefaction features found at a site in western Tennessee. Two near-surface seismic reflection profiles, chosen to cross sand blows found at the site, were collected for this study. The new seismic reflection data reveal near-surface deformation consistent with the presence of the earthquake-induced liquefaction deposits, but lack evidence for shallow faulting beneath the site. Rather, deformation observed in the seismic lines is consistent with lateral spreading that may have occurred during an episode of strong ground shaking. The trend of liquefaction features, however, is parallel to a system of northeast-southwest-trending faults and supports the interpretation that the subsurface deformation seen in the reflection data may reflect active faulting nearby.

Acknowledgments

I would like to thank my thesis advisor, Dr. Lorraine Wolf for her support throughout this entire project. I would also like to thank Dr. Martitia Tuttle, Dr. Mark Steltenpohl, and Dr. Stephanie Shepherd for their insight and contributions. Their support during this process proved to be extremely beneficial and I am very grateful.

I cannot thank my family and friends enough for their encouragement, support, and sacrifices they have given me throughout my life. They have truly helped mold me into the man I am today. There will always be a special place in my heart for Auburn University and the lasting friendships I have made here.

Figure Captions

Figure 1: Map of New Madrid seismic zone, showing location, size, and estimated ages of measured liquefaction features (Tuttle et al., 2002; M. Tuttle pers. communication, 2018). Surface area of sand blows is from Saucier (1991) and Obermeier et al. (2000). Study site shown by yellow star.

Figure 2: Generalized cross-section and stratigraphic column of post-Paleozoic sediments along the Arkansas-Tennessee border (Hardesty, 2008).

Figure 3: Conductivity logs along profile k-k' (see Figure 5) near Pritchett site at southern end of the Reelfoot rift. Vertical offsets of Cockfield formation tops are interpreted as faults (Martin et al., 2017).

Figure 4: Map of NMSZ, showing known faults (blue lines) and locations of liquefaction sites (red dots) in relation to the Pritchett site (gold star); Orange polygons show sand blow deposits. EM—Eastern Rift Margin faults, AF—Axial fault, WM—Western Rift Margin fault, all other abbreviations as in Csontos et al. (2008).

Figure 5: Location of K-K' (see Figure 3) in relation to northeast-striking faults and northwest-striking Reelfoot fault (Martin et al., 2017). Pritchett site indicated by gold star.

Figure 6: Google Earth© image of Pritchett site showing location of seismic reflection surveys (red lines), electrical resistivity surveys (green lines), and trenches (yellow lines) (M. Tuttle pers. communication 2017).

Figure 7: Data from electrical resistivity surveys; A-C denote three west-east parallel profiles spaced 5 m apart north to south (see Figure 6). Dots along top indicate position of 48 electrodes spread at 2 m intervals. Large sand dike locations are indicated by black lines. High resistivity areas are shown in blue and more conductive areas in red (Wolf, personal communication, 2016). Brackets in panel C indicate trench 1 (left) and trench 2 (right) (see Figure 8).

Figure 8: Trench logs showing the location and geometry of sand dikes and sand blows. Trench locations are shown on Figure 6 and on profile C of Figure 7. (Tuttle, personal communication, 2016).

Figure 9: Flow chart showing all processing steps for seismic lines 1 and 2.

Figure 10: Shot gathers showing before and after near-offset traces were deleted.

Figure 11: Shot gather from seismic line 1 without (left) and with early mute (right).

Figure 12: Shot gather from seismic line 2 without (left) and with late mute (right).

Figure 13: Example of a CMP gather showing tests of different velocities for the NMO correction. Each panel (left to right) contains data processed with different (increasing) velocities for the NMO correction, starting with 700 m/s and ending with 1300 m/s. Second panel from right shows flattening of a reflection indicated by the red line.

Figure 14: Flow chart for NMO correction on seismic line 1.

Figure 15: Seismic line 1, muted shot gather (left) and stacked NMO-corrected CMP profile.

Figure 16: Seismic line 2, muted shot gather (left) and stacked NMO-corrected CMP profile.

Figure 17: Plots showing signal spectrum before (top) and after (bottom) whitening the frequency spectrum.

Figure 18: NMO stacked (upper panel) and deconvolved (lower panel) data for seismic line 1.

Figure 19: NMO stacked (upper panel) and deconvolved (lower panel) data for seismic line 2.

Figure 20: Deconvolved stack without (upper panel) and with (lower panel) with bandpass filter applied for seismic line 1.

Figure 21: Deconvolved stack without (upper panel) and with (lower panel) bandpass filter applied for seismic line 2.

Figure 22: Seismic line 1 without (upper panel) and with (lower panel) static correction applied.

Figure 23: Seismic line 2 without (upper panel) and with (lower panel) static correction applied.

Figure 24: Seismic reflection line 1, with signal disruptions at CMP locations 117-121 and 137-141 (shown in red circles).

Figure 25: Seismic reflection line 2, with disrupted reflections between CMP locations 113-119 (shown in red circle).

Figure 26: Seismic reflection line 1 with locations of sand blow deposits at surface labeled. Note disrupted reflections between locations roughly 116-119 and 137-141.

Figure 27: Seismic reflection line 2 with locations of sand blow deposits at surface labeled. Note disrupted reflections between locations roughly 115-118 and 135-138.

Figure 28: Pritchett site map showing location of seismic reflection surveys (red lines), with blue dots indicating positions of disrupted reflections on profiles (Figures 26 and 27) overlain on sand blows. Note two different orientations of sand blow deposits (see Discussion). Also shown are locations of electrical resistivity surveys (green lines) and trenches (yellow lines).

Table of Contents

Abstract	i
Acknowledgments.....	ii
Figure Captions.....	iii
Introduction.....	1
Geologic Background.....	3
Previous Work.....	4
The Pritchett Study Site.....	7
Methodology	10
Seismic Data Acquisition.....	10
Seismic Data Processing.....	11
Seismic Line Geometry.....	12
Muting.....	13
Normal Moveout.....	14
Deconvolution/Whitening.....	14
Bandpass Filtering.....	18
Residual Static Correction.....	20
Final Processed Seismic Sections.....	21
Discussion.....	23
Conclusions.....	25
References.....	27
Appendices.....	29
Appendix A.....	30
Appendix B.....	34

Introduction

The New Madrid seismic zone (NMSZ) is located along the shared border of northeast Arkansas, western Tennessee, southeastern Missouri, and southwestern Kentucky (Figure 1). This area of North America is at the center of a failed rift system, which subsided and filled with sediment to form the Mississippi Embayment (Burke and Dewey, 1973). Due to the thick accumulation of sediments now present in the embayment, faults and structures associated with the rifting are deeply buried. Although current seismicity is mostly of low magnitude within the NMSZ, the area is widely known for three earthquake sequences that occurred in 1811 and 1812 with estimated moment magnitudes of $M > 7$ (Tuttle et al., 2002; M. Tuttle, pers. communication, 2018). These earthquakes are some of the largest in United States history and caused widespread soil liquefaction throughout the Mississippi Embayment (Obermeier and Dickenson, 2000).

Earthquake-induced liquefaction deposits are used by paleoseismologists to study prehistoric earthquakes and to estimate recurrence intervals of large earthquakes. Paleoseismic studies of liquefaction deposits in the NMSZ suggest that at least three seismic events similar to the 1811-1812 earthquake sequence occurred between A. D. 200 and 1670 (Tuttle et al., pers. communication; Tuttle et al., 2002). Based on these studies, it has been estimated that large earthquake sequences occur in ~ 400- to 500-year intervals (Tuttle et al., 2002). To date, over 250 liquefaction sites have been investigated in the NMSZ (Liu and Li, 2001). Several of these sites are located along the Obion River, a small tributary of the Mississippi River. The number and orientation of liquefaction deposits along the Obion River suggest that an active fault may be present beneath the floodplain. This study focuses on a site along the Obion River located near Dyersburg, Tennessee, herein referred to as the Pritchett site (Figure 1). The purpose of this research is to determine whether liquefaction deposits observed at the site are related to the existence of an active fault at depth.

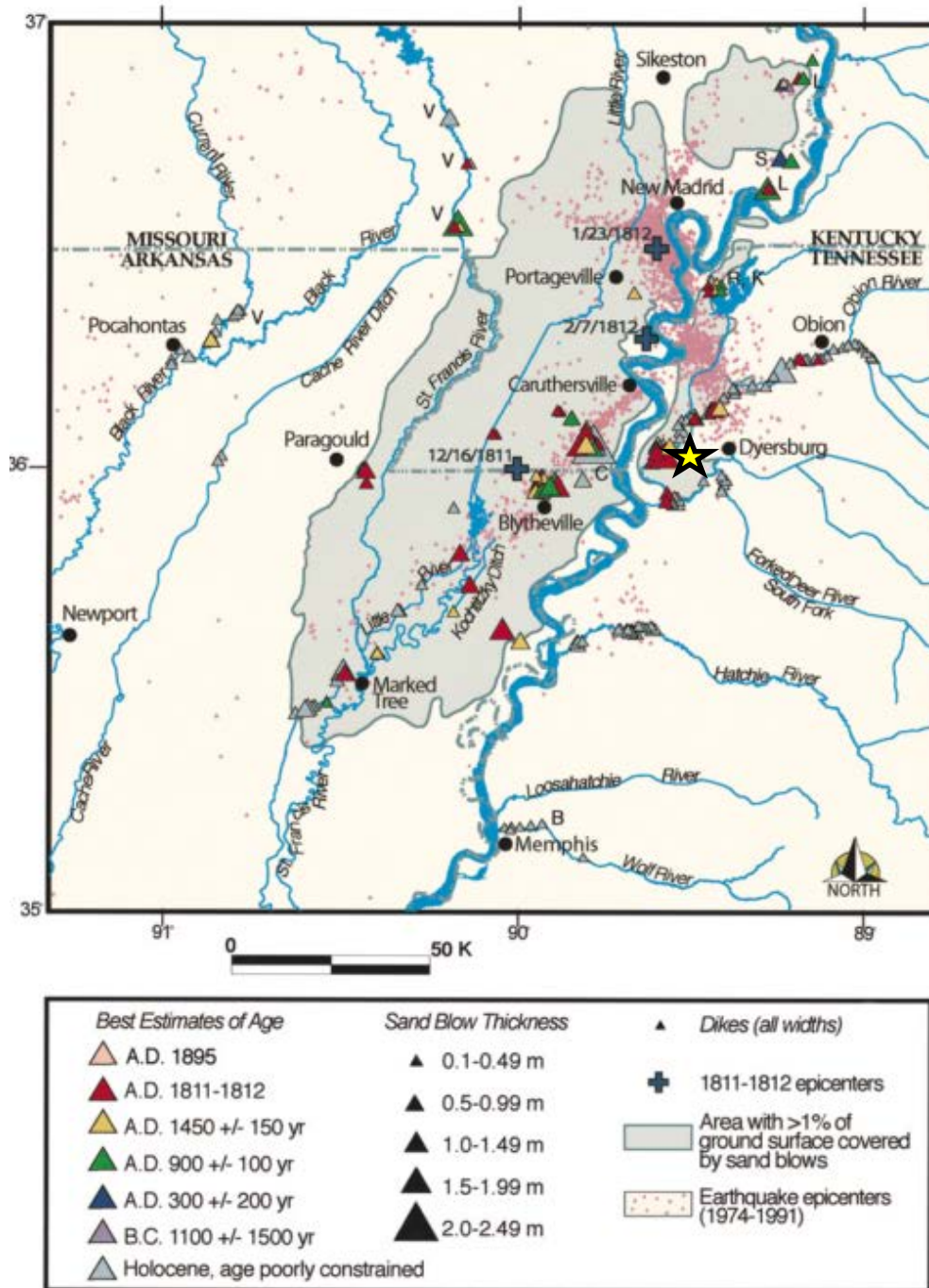


Figure 2: Map of New Madrid seismic zone, showing location, size, and estimated ages of measured liquefaction features (Tuttle et al., 2002; M. Tuttle pers. communication, 2018). Surface area of sand blows is from Saucier (1991) and Obermeier et al. (2000). Study site shown by yellow star.

Geologic Background

The Mississippi Embayment sits above a northeast-striking graben that is approximately 65 km wide and 320 km long (Hildenbrand, 1985). Based on an interpretation of gravity data, Burke and Dewey (1973) postulated that the Mississippi embayment most likely originated as a Mesozoic failed-arm rift, which we now know as the Reelfoot rift. The formation of the Reelfoot rift began during the late Precambrian or early Paleozoic, and was later reactivated in the Cretaceous (Hildenbrand, 1985). Rifting began with the opening of the Iapetus ocean, where extension was followed by a period of subsidence and down-warping. This deformation introduced an inland seaway into which sediments were deposited. The rift was filled with Cambrian-aged marine sediments (Howe and Thompson, 1984) and later unconformably overlain by Cretaceous and younger shallow marine and alluvial clastic sediments (Figure 2) (Luzietti et al., 1992) as described below.

The Cretaceous McNairy Formation is a fine to coarse-grained sand with interbedded layers of clay (Figure 2). Overlying the McNairy Formation is the Paleocene Porters Creek Clay, a hard micaceous clay that acts as a confining unit to produce overpressures in the embayment (Van Arsdale and TenBrink, 2000; Wolf et al., 2005). Above the Porters Creek Clay lies Eocene alluvial sediments consisting of the Fort Pillow Sand and the Flour Island Formation, which are described as sandy micaceous silty clays (Van Arsdale and TenBrink, 2000). The Eocene Memphis Sand lies above the Flour Island Formation and is described as coarse sand with interbedded clay and silt (Martin et al., 2017). Directly above the Memphis Sand lies the Eocene Cook Mountain Formation, which consists primarily of sands with clays and silts (Figures 2 and 3). Above the Cook Mountain Formation is the Cockfield Formation consisting of sand, silt, clay, and lignite. The thin, Pliocene-age Upland Complex, composed of very coarse-grained,

cross-bedded sands lies above the Cockfield Formation and is topped by Quaternary alluvium (Martin et al., 2017). In western Tennessee, precise formation top locations are provided from Martin et al. (2017) and Van Arsdale and TenBrink (2000).

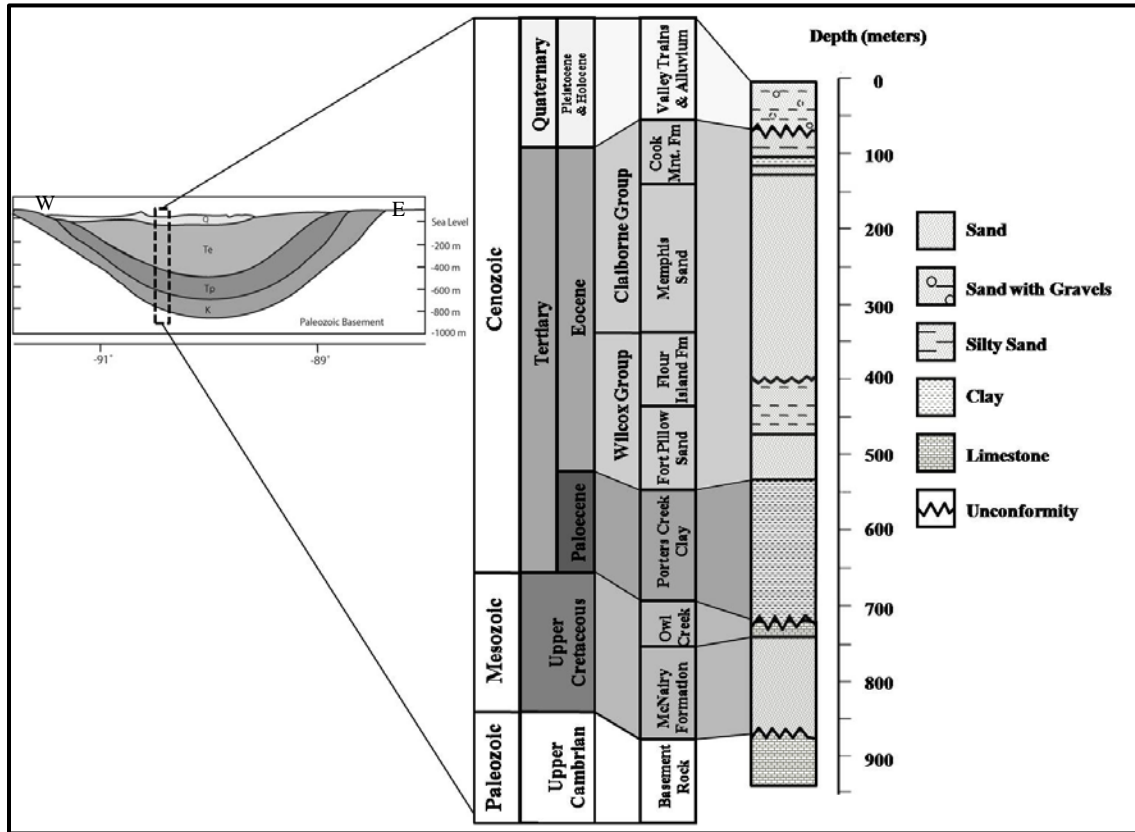


Figure 2: Generalized cross-section and stratigraphic column of post-Paleozoic sediments along the Arkansas-Tennessee border (Hardesty, 2008).

Previous work

Several seismic surveys have been conducted to explore the structure of the Reelfoot rift and to image potentially active faults (Figures 4 and 5). In 1991, a seismic reflection study was conducted across the northern Mississippi Embayment as part of the Consortium for Continental Reflection Profiling (COCORP) project (Nelson and Zhang, 1991). The experiment revealed faults related to the late Precambrian/early Paleozoic Reelfoot rift. The study suggested the

possibility that the Reelfoot rift formed along the southern extension of the Grenville Front (Nelson and Zhang, 1991). In 1999, Woolery et al. conducted seismic reflection surveys in the Kentucky bend area of the NMSZ to map near-surface neotectonic structures, which revealed a style and geometry of deformation features consistent with documented regional faults (Woolery et al., 1999). More recently, Csontos et al. (2008) analyzed 1,704 earthquake hypocenters to map fault geometry in the NMSZ; this study suggested that the northwest-trending Reelfoot fault is a southwest-dipping reverse fault that extends across the entire width of the Reelfoot rift and produces most of the seismicity in the NMSZ (Figure 5).

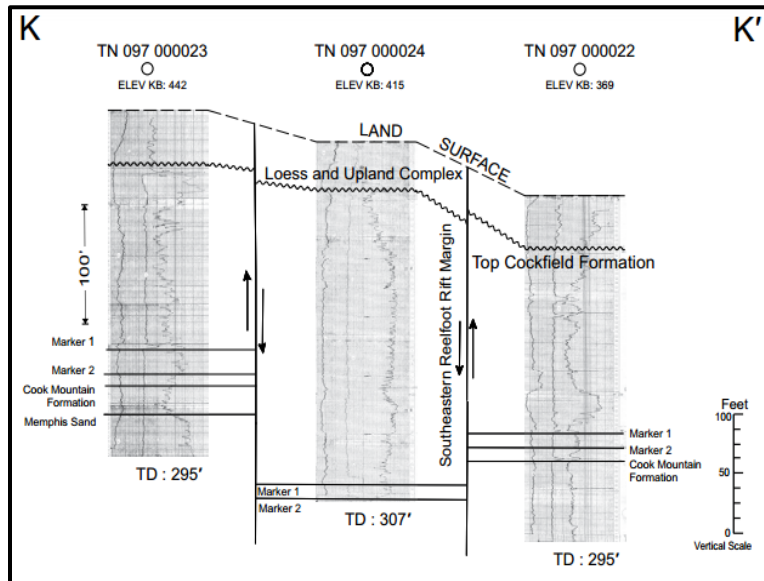


Figure 3: Conductivity logs along profile k-k' (see Figure 5) near Pritchett site at southern end of the Reelfoot rift. Vertical offsets of Cockfield formation tops are interpreted as faults (Martin et al., 2017).

Although seismic profiles have elucidated sections of the faults within the NMSZ, the major indicator of neotectonic fault activity within the zone is the current trend in seismicity. Two parallel branches of seismicity-oriented northeast-southwest demarcate the margins of the Reelfoot rift, the principal structure underlying the embayment (Figure 1).

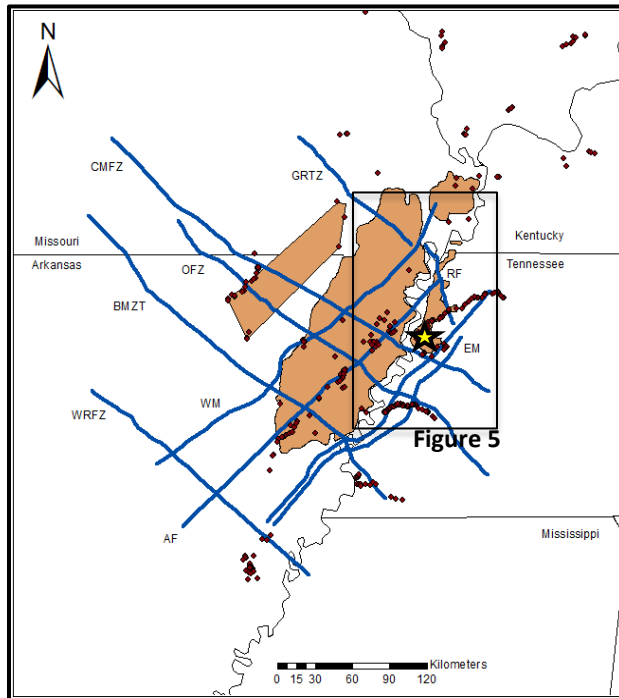


Figure 4: Map of NMSZ, showing known faults (blue lines) and locations of liquefaction sites (red dots) in relation to the Pritchett site (gold star); Orange polygons show sand blow deposits. EM—Eastern Rift Margin faults, AF—Axial fault, WM—Western Rift Margin fault, all other abbreviations as in Csonotos et al. (2008).

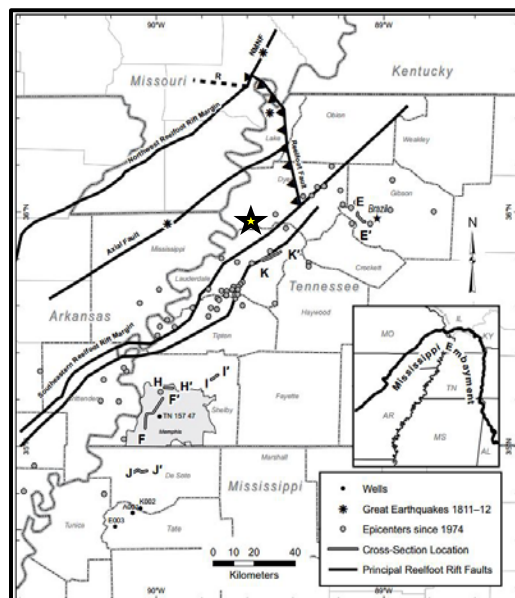


Figure 5: Location of K-K' (see Figure 3) in relation to northeast-striking faults and northwest-striking Reelfoot fault (Martin et al., 2017). Pritchett site indicated by gold star.

The most common surface deformation features related to earthquakes found in the NMSZ are liquefaction features, which include sand dikes and sand blows. The occurrence of these earthquake-induced features is important because they typically form in earthquakes of $M > 6$. In addition to the shaking required for liquefaction, there are other criteria, such as sediment composition, that govern liquefaction. Liquefaction is most likely to occur in saturated, clean sand layers that are buried beneath a nonliquefiable layer with low permeability (Obermeier et al., 2000); however, there have been instances of fine and coarse-grained sources as well. The process of liquefaction starts with cyclic strain caused by strong ground motion. Given favorable stratigraphic conditions, these motions cause a realignment of grains in the saturated sand layer. Fluid pressure then builds if a confining layer is present that inhibits the release of pressure. Once the fluid pressure exceeds the lithostatic pressure, the water-saturated sand will escape upwards following a path of least resistance, and deposit on the surface as a sand blow (Obermeier and Dickenson, 2000).

The Pritchett Study Site

The Pritchett site is located near the eastern margin of the Reelfoot rift, approximately 160 km northeast of Memphis and within 10 km of the Mississippi River (Figure 1). The area hosts several northeast-striking faults: the Eastern Rift Margin faults, the Axial fault, and Western Rift Margin fault (Figures 4 and 5). These fault systems have been interpreted as normal faults (Nelson and Zhang, 1991) and are intersected by northwest-striking thrust faults (Csontos et al., 2008).

The Pritchett site was discovered during field reconnaissance along the Obion River (Tuttle, personal communication, 2016). A large sand dike and buried sand blow were found in the riverbank directly to the north of the Pritchett site. The surface expression of sand blows and sand fissures observed in satellite imagery of the site had a similar orientation to the northeasterly strike of the discovered sand dike (Figure 6), suggesting that the two features might be related to a larger structure. Both follow a similar trend to the regional northeast-trending fault systems (Figures 4 and 5). In 2011, a single seismic reflection survey was conducted on the floodplain north of the dike location (L. Wolf, pers. communication, 2016). A shorter version of this seismic line was repeated in 2015 (Martin, 2014). Data from these lines did not yield evidence of a fault, although only preliminary processing was performed on the data.

In 2015, Tuttle and others conducted additional reconnaissance surveys on sand blows at the Pritchett site (Figure 6) (Tuttle et al., personal communication, 2016). The initial reconnaissance included digging soil test pits and conducting an archeological assessment. As part of the reconnaissance, electrical resistivity surveys were collected at the Pritchett site and another location 0.5 km to the south (Figures 6 and 7; L. Wolf, personal communication, 2016). The purpose of these surveys was to image feeder dikes for the sand blows and possibly the source layer. All surveys were oriented east-west, crossing several sand fissures. Figure 7 shows the results from three parallel profiles located in the northwest quadrant of the site (Figure 6). Data from the southern survey are not shown here. The data from the Pritchett resistivity profiles showed the presence of two sand dikes, which were confirmed during trenching (Figures 7 and 8) (Tuttle, personal communication, 2016).

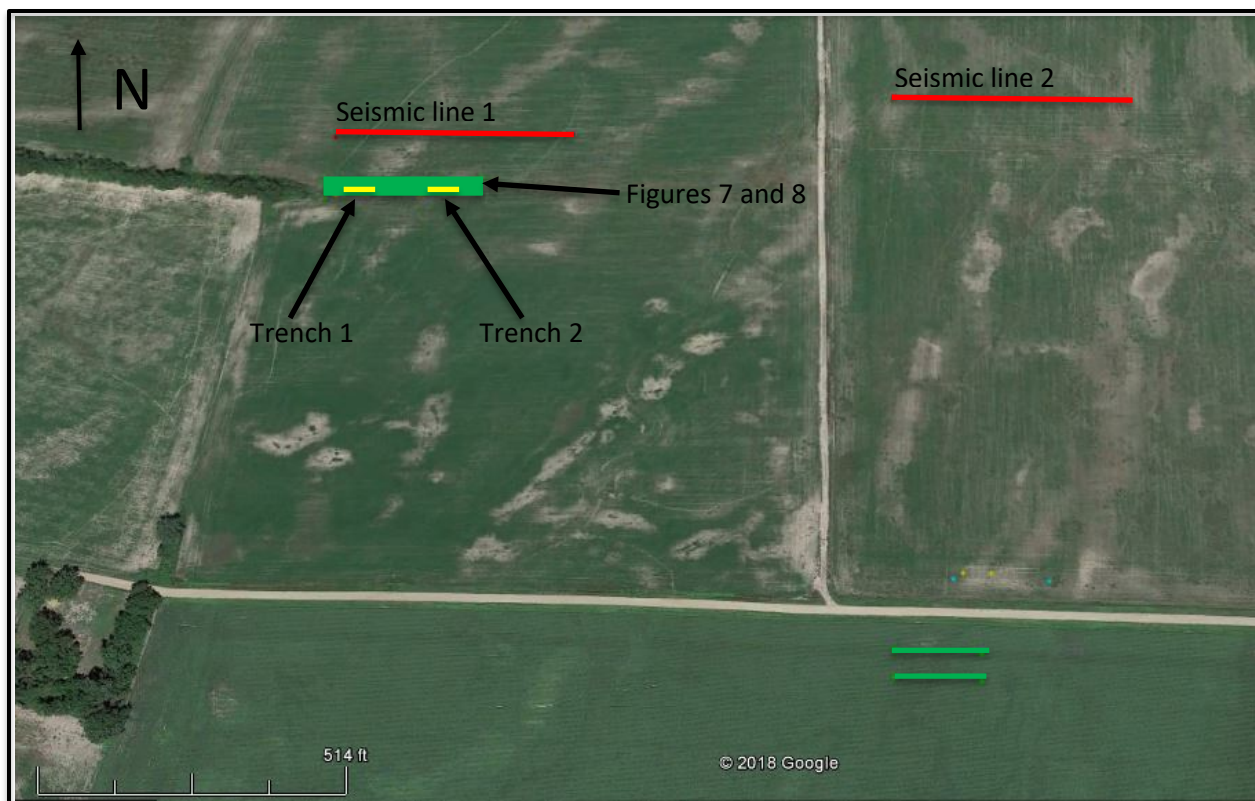


Figure 6: Google Earth© image of Pritchett site showing location of seismic reflection surveys (red lines), electrical resistivity surveys (green lines), and trenches (yellow lines) (M. Tuttle pers. communication 2017).

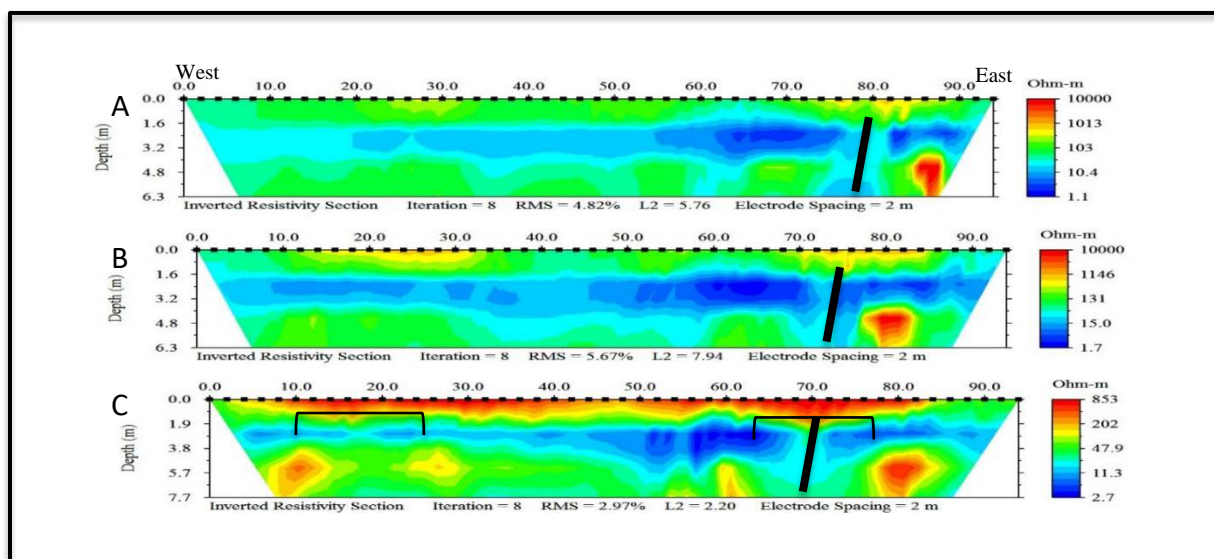


Figure 7: Data from electrical resistivity surveys; A-C denote three west-east parallel profiles spaced 5 m apart north to south (see Figure 6). Dots along top indicate position of 48 electrodes spread at 2 m intervals. Large sand dike locations are indicated by black lines. High resistivity areas are shown in blue and more conductive areas in red (Wolf, personal communication, 2016). Brackets in panel C indicate trench 1 (left) and trench 2 (right) (see Figure 8).

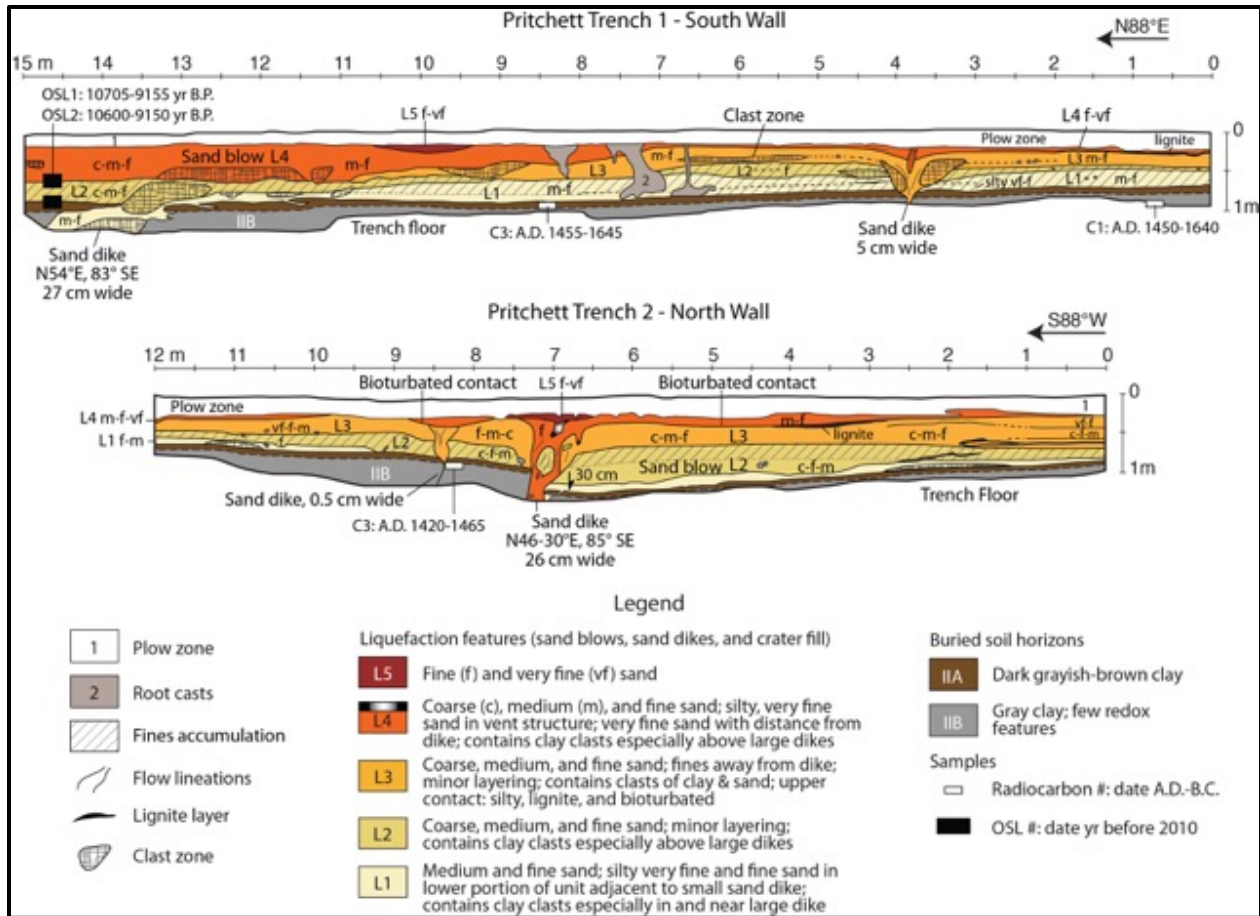


Figure 8: Trench logs showing the location and geometry of sand dikes and sand blows. Trench locations are shown on Figure 6 and on profile C of Figure 7 (Tuttle, personal communication, 2016).

Methodology

This section describes the data acquisition and processing methods of this study. Data acquisition involved selecting the profile lines and acquiring seismic reflection data. Data processing involved analyzing and manipulating the seismic reflection data.

Seismic Data Acquisition

Two profiles, 151 m in length, were selected for the seismic survey. The lines were positioned to cross NE-SW striking sand blows visible on the surface and to run parallel to the

electrical resistivity profiles (Figure 6). Seismic reflection data were acquired using a Geometrics Strataview 48-channel seismometer with 30-Hz geophones, a steel plate, and a 4.5-kg sledgehammer. Each source shot was recorded on 24 channels, then the geophone sequence was rolled to the next shot location. Shots were taken every 3 m for a total of 51 shots. The geophones were spaced in 3-m intervals, with a 9-m shot offset in an attempt to avoid surface wave energy at near offsets. The sampling interval used for acquisition was 125 μ s for 1280 ms per shot. Details on survey geometry is given in Appendix A. Seismic data collected for this study is available as an electronic supplement (see Appendix B for details).

Seismic Data Processing

The Parallel Geosciences seismic data processing program, Seismic Processing Workshop (SPW)TM, was used to process the data. Processing steps included assigning geometry values, muting, normal moveout correction, deconvolution/whitening, bandpass filtering, and residual static correction of the data. All data processing steps are performed through data “flows” that direct processing steps; an example of a flow chart is shown in Figure 9. An example of a typical shot gather is shown in Figure 10. The unprocessed data show the dominance of surface waves at close offsets and the presence of high frequency noise. In order to obtain an optimum offset for reflection and remove surface wave noise, near offset traces from station locations less than 36 m from the shot point were deleted (Figure 10).

Seismic Line Geometry

Seismic data are acquired in SEG-2 format on the Strataview seismograph. These data must be reformatted for use in SPW. After the data are reformatted, the geometry describing the experimental setup (e.g., shot spacing, geophone spacing, station spacing, etc.) must be assigned.

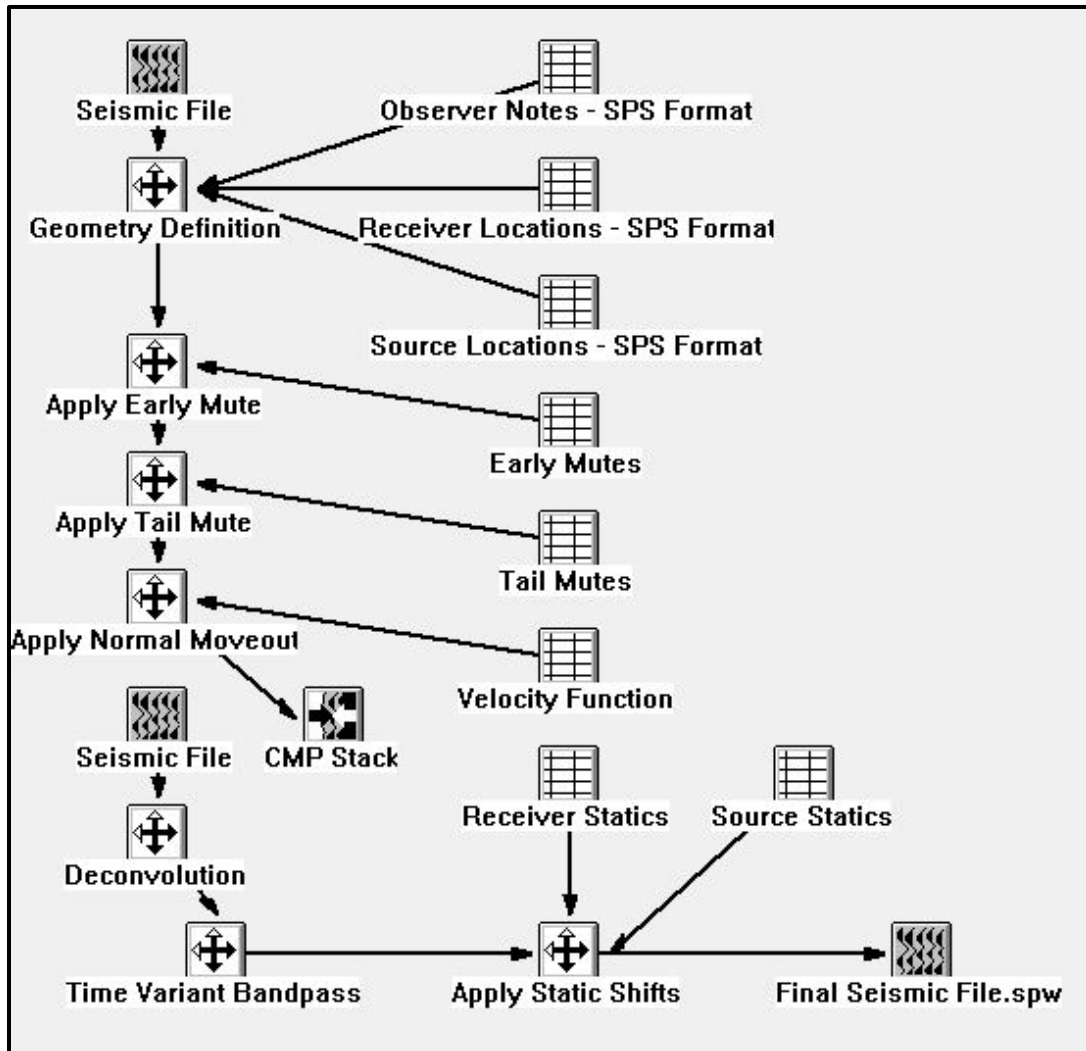


Figure 9: Flow chart showing all processing steps for seismic lines 1 and 2.

Muting

Both early and late mutes were applied to eliminate as much surface wave energy and noise as possible from the data. The early mute is used to eliminate the direct arrival and the refracted head wave. An early mute takes a specified time and mutes all data before it, whereas a late mute designates a time and mutes all data arriving after that time. Figures 11 and 12 show the application of the mutes.

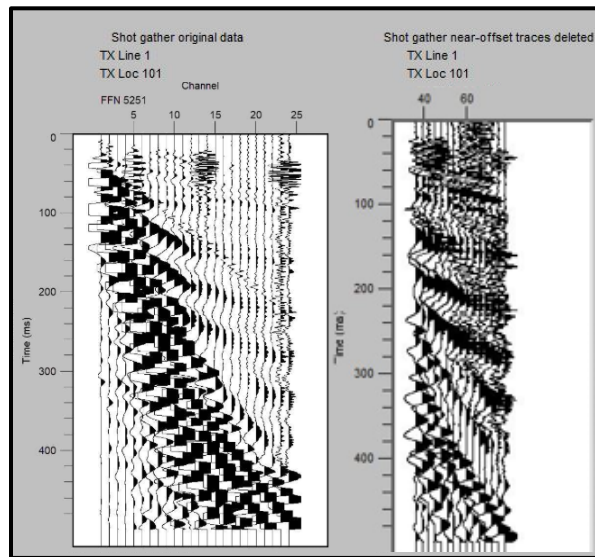


Figure 10: Shot gathers showing before (no geometry) and after near-offset traces were deleted.

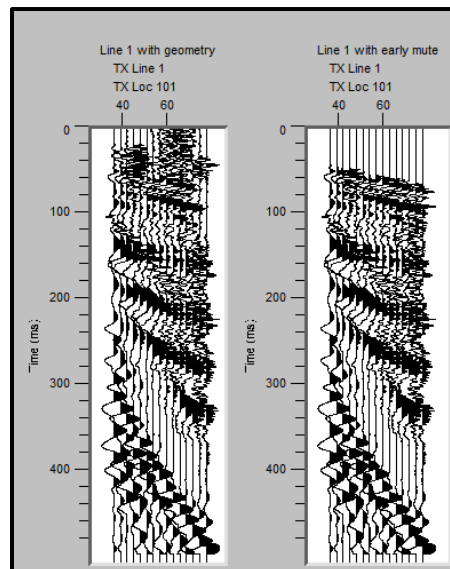


Figure 11: Shot gather from seismic line 1 without (left) and with early mute (right).

Normal Moveout

A normal moveout correction (NMO) is the difference taken from the travel time along an oblique reflection ray path minus the time required for the normal incident ray path and depends on velocity (Burger, 2006). To determine which velocities to use for the correction, it is useful to test multiple constant velocity NMOs. NMOs are performed on common-midpoint gathers (CMP), which consist of all traces in the experiment that sample the same subsurface location. The goal of the NMO correction is to remove the variation in arrival time due to different raypath lengths of traces within the gather, so that the traces can be convolved (added together) to increase the signal to noise ratio. Because velocity typically increases with depth, reflections observed in the data may require different velocities for the NMO correction. The correct velocity is achieved when an individual reflection in a CMP gather becomes flattened (Figure 12). A preliminary stack is used to determine further processing steps. For this project, a constant velocity NMO correction of 1200 m/s deemed sufficient for the processing (Figures 13, 14, and 15).

Deconvolution/Whitening

Deconvolution is the process of restoring the source wavelet to an approximation of the shot pulse, while also removing multiples. The NMO-corrected data are deconvolved using user-specified parameters for pre-whitening, filter length, design window length, and type of deconvolution (predictive or spiking). These parameters are selected by viewing the frequency spectrum of the data using the vector calculator (Figure 16). Once the parameters have been selected, the whitening process boosts all frequencies to approximately the same level (flattening the spectrum). Figures 17 and 18 show the data from the profiles, respectively, after deconvolution is applied.

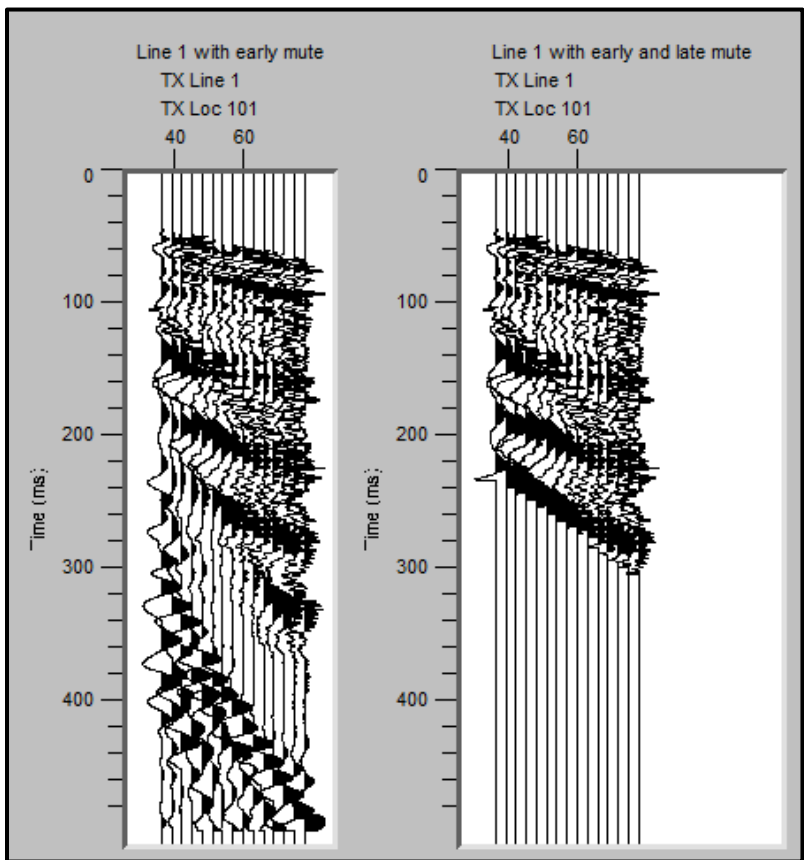


Figure 12: Shot gather from seismic line 2 without (left) and with late mute (right).

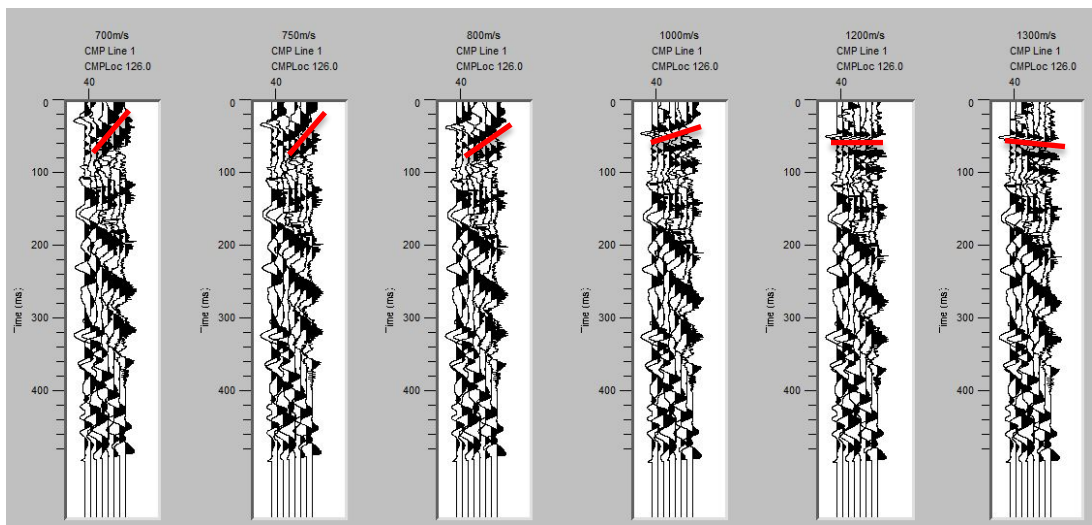


Figure 13: Example of a CMP gather showing tests of different velocities for the NMO correction. Each panel (left to right) contains data processed with different (increasing) velocities for the NMO correction, starting with 700 m/s and ending with 1300 m/s. Second panel from right shows flattening of a reflection indicated by the red line.

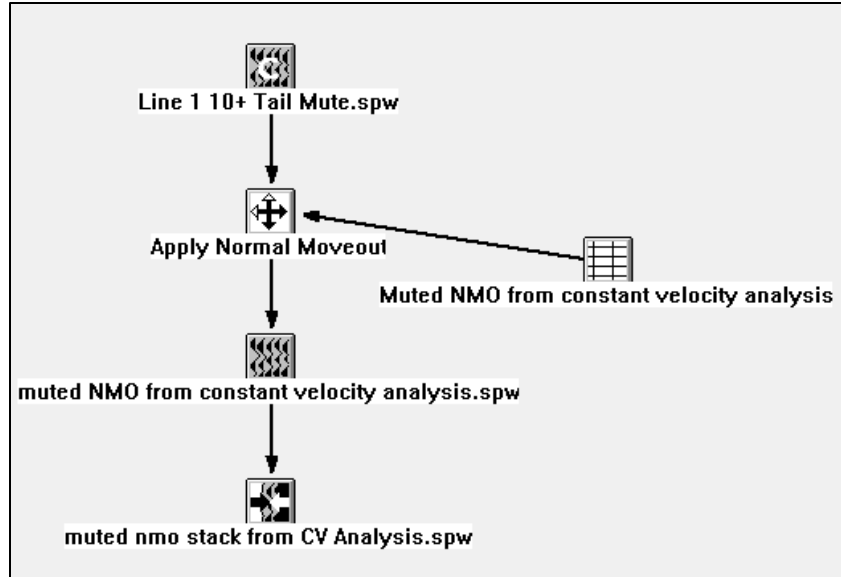


Figure 14: Flow chart for NMO correction on seismic line 1.

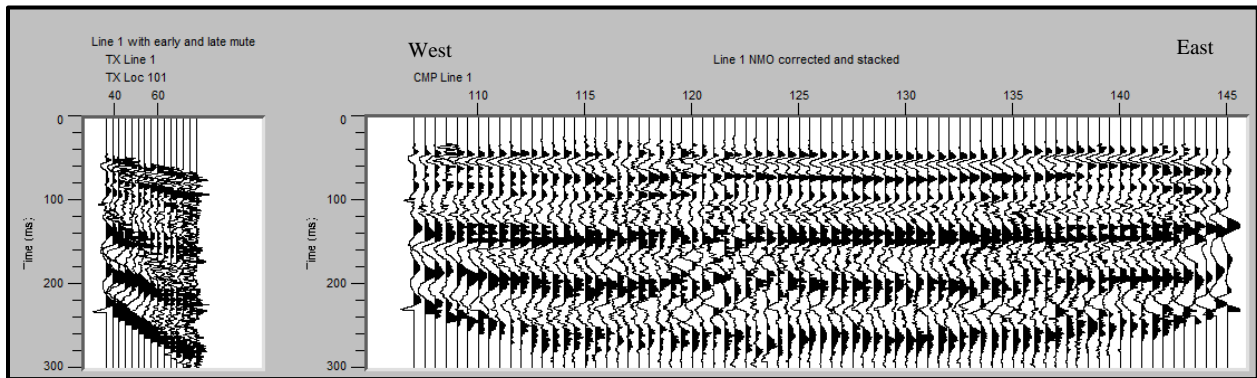


Figure 15: Seismic line 1, muted shot gather (left) and stacked NMO-corrected CMP profile.

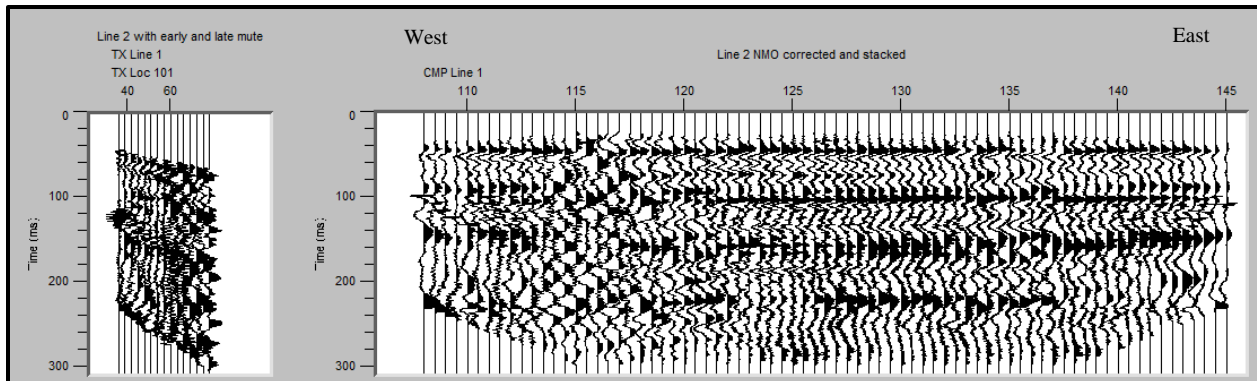


Figure 16: Seismic line 2, muted shot gather (left) and stacked NMO-corrected CMP profile.

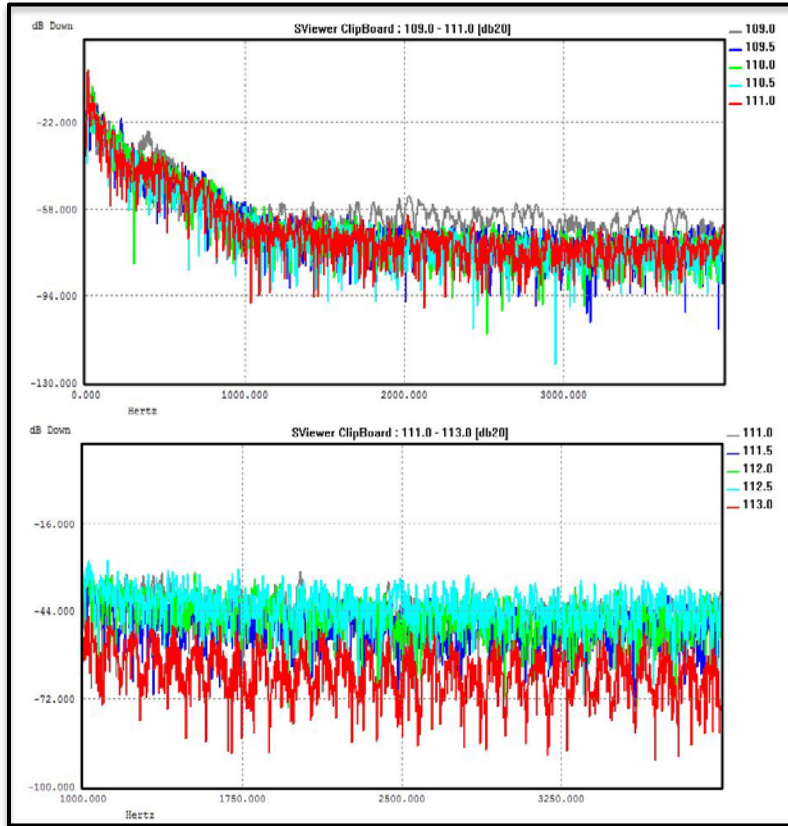


Figure 17: Plots showing signal spectrum before (top) and after (bottom) whitening the frequency spectrum.

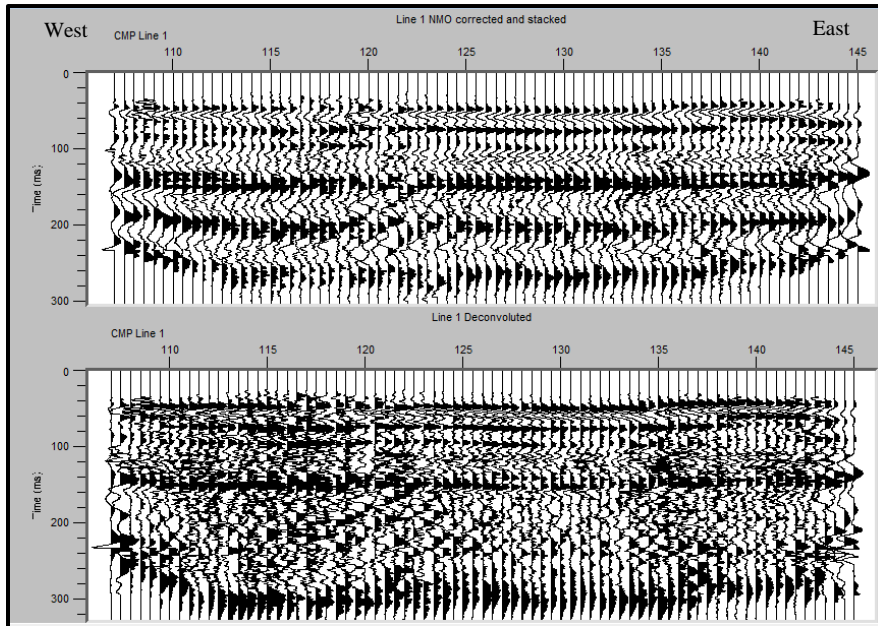


Figure 18: NMO stacked (upper panel) and deconvolved (lower panel) data for seismic line 1.

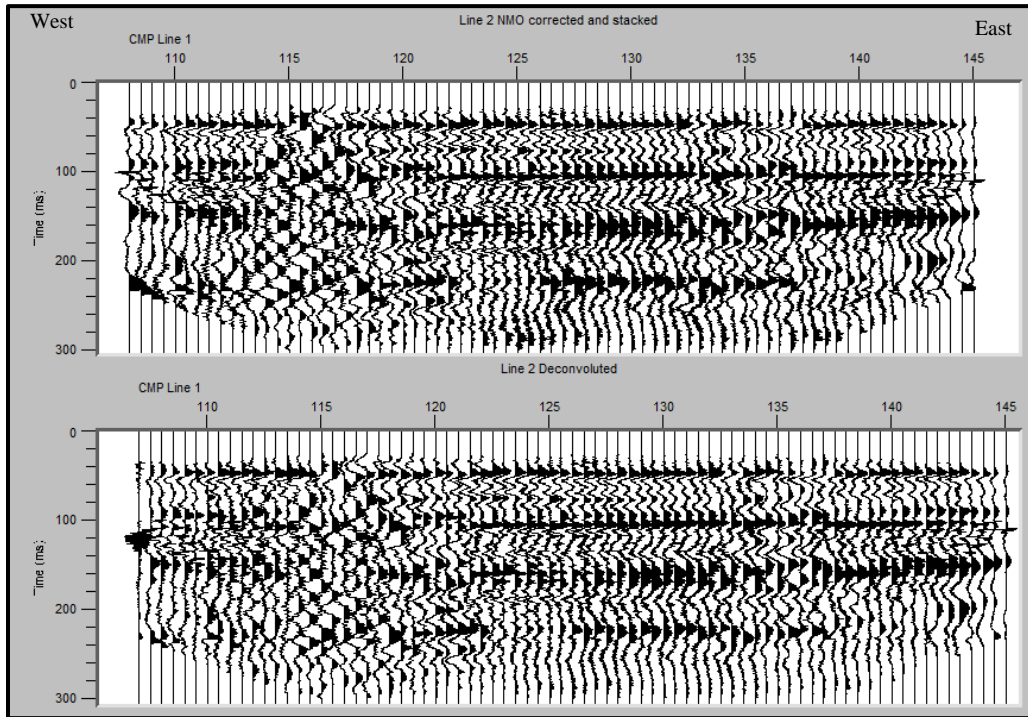


Figure 19: NMO stacked (upper panel) and deconvolved (lower panel) data for seismic line 2.

Bandpass Filtering

The process of spectral whitening introduces high-frequency noise into the data because it boosts amplitudes across all frequency bands. A bandpass filter was applied to the data to reduce noise in undesirable frequency bands. Bandpass filtering is the use of both high and low-cut filters applied to a certain range of time in the data record. The filter used was a low-cut of 0 to 15 Hz and a high-cut of 50 to 250 Hz. These frequencies were selected based on the frequency analysis from the deconvolution process. The results of the bandpass filter are shown below (Figures 20 and 21).

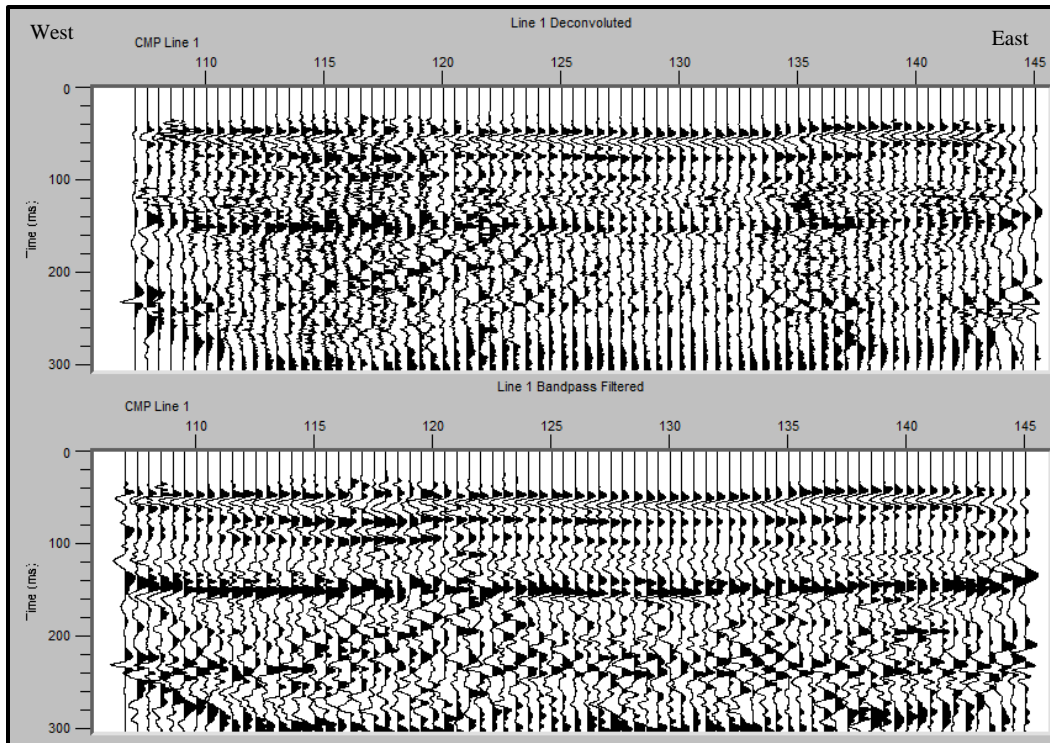


Figure 20: Deconvolved stack without (upper panel) and with (lower panel) with bandpass filter applied for seismic line 1.

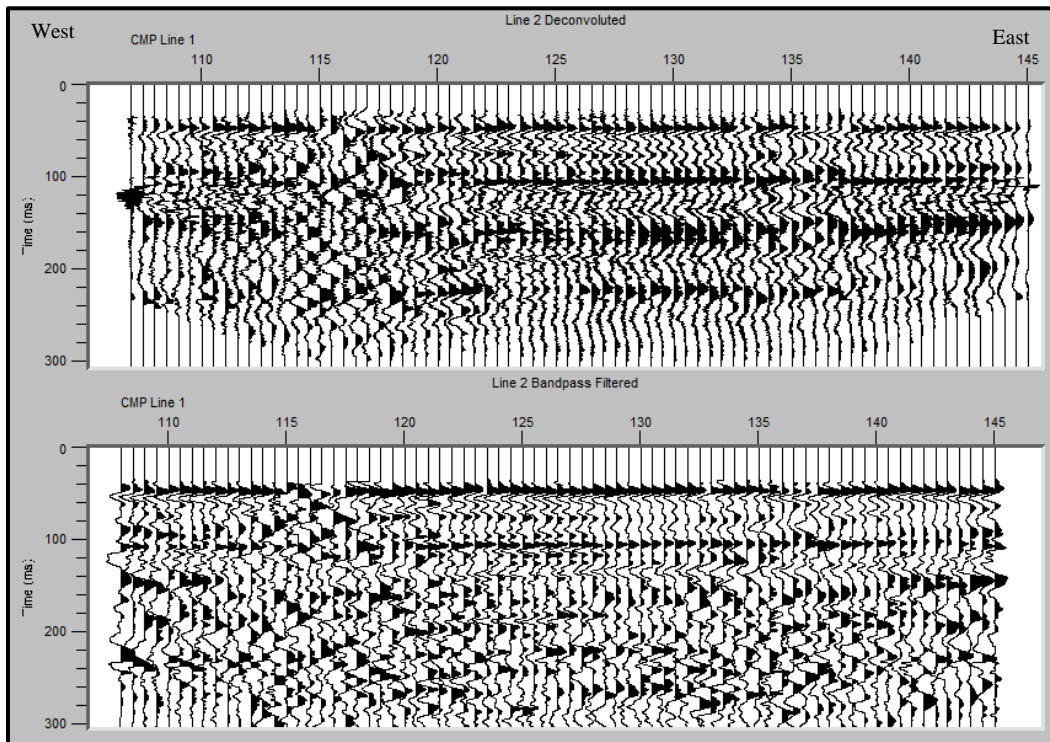


Figure 21: Deconvolved stack without (upper panel) and with (lower panel) bandpass filter applied for seismic line 2.

Residual Static Correction

A residual statics correction is used to adjust each trace to account for arrival time differences caused by waves travelling through the weathered layer. It uses a travel-time model that assumes vertical ray paths through the near surface weathered layer, which means that a ray arriving from any azimuth will travel the same path through the weathered layer to reach a station location. Because both negative and positive shifts are just as likely to occur, the average amount of shift will tend to zero. Traces within the stacked data can be compared by cross-correlation to a pilot trace in order to establish time differences between the traces. Results from the residual static correction are shown below (Figures 22 and 23).

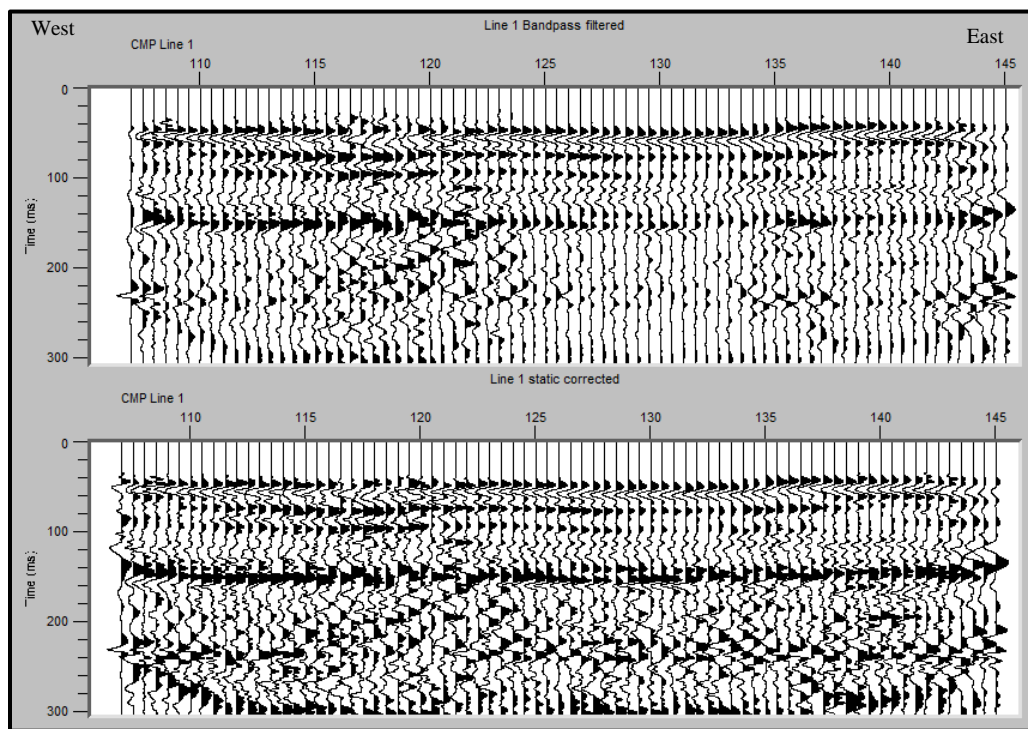


Figure 22: Seismic line 1 without (upper panel) and with (lower panel) static correction applied.

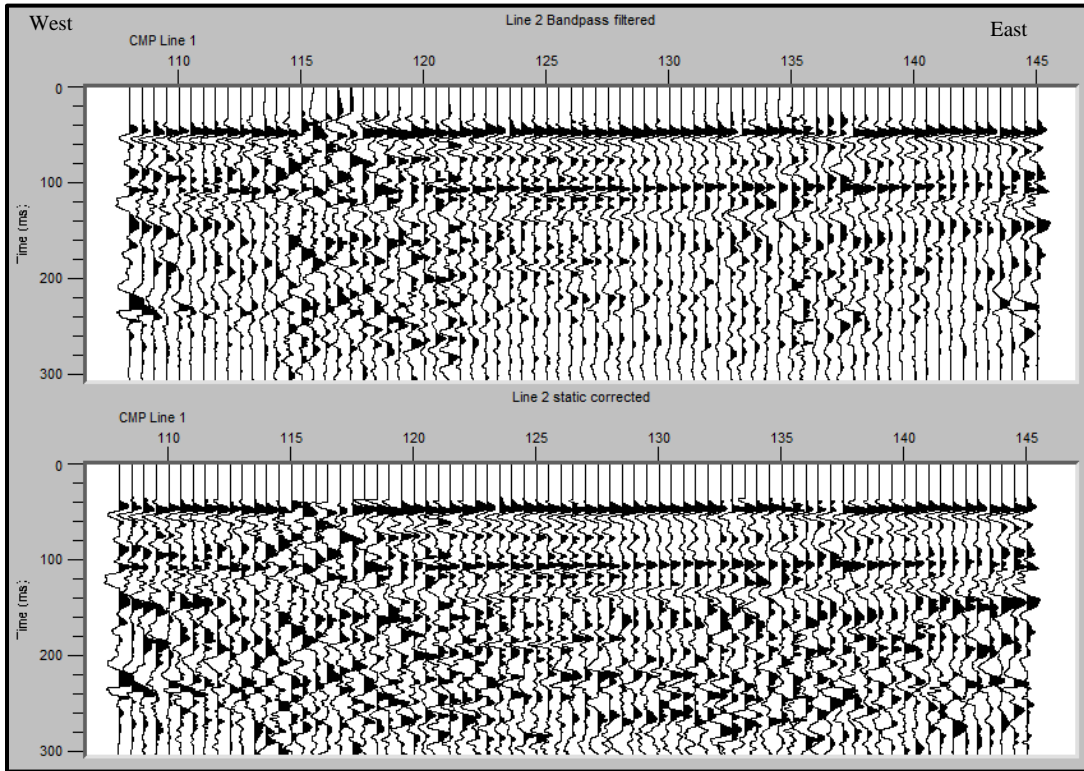


Figure 23: Seismic line 2 without (upper panel) and with (lower panel) static correction applied.

Final Processed Seismic Sections

Figure 24 shows the final processed data collected from seismic line 1. There are four distinct reflectors visible between 40 ms and 160 ms, with the latter two showing a disruption of signal near CMP location 120. Between CMP locations 137-141, the uppermost reflector exhibits an anticlinal bend, with the second and third reflectors showing offset of ~15 to 20 ms. The deepest reflection (~140 ms) indicates little if any deformation. Both areas along the profile are collocated with the locations of sand blows observed at the surface and slightly north of the liquefaction features (sand blows and dikes) revealed in the electrical resistivity surveys and trench logs (Figures 7 and 8).

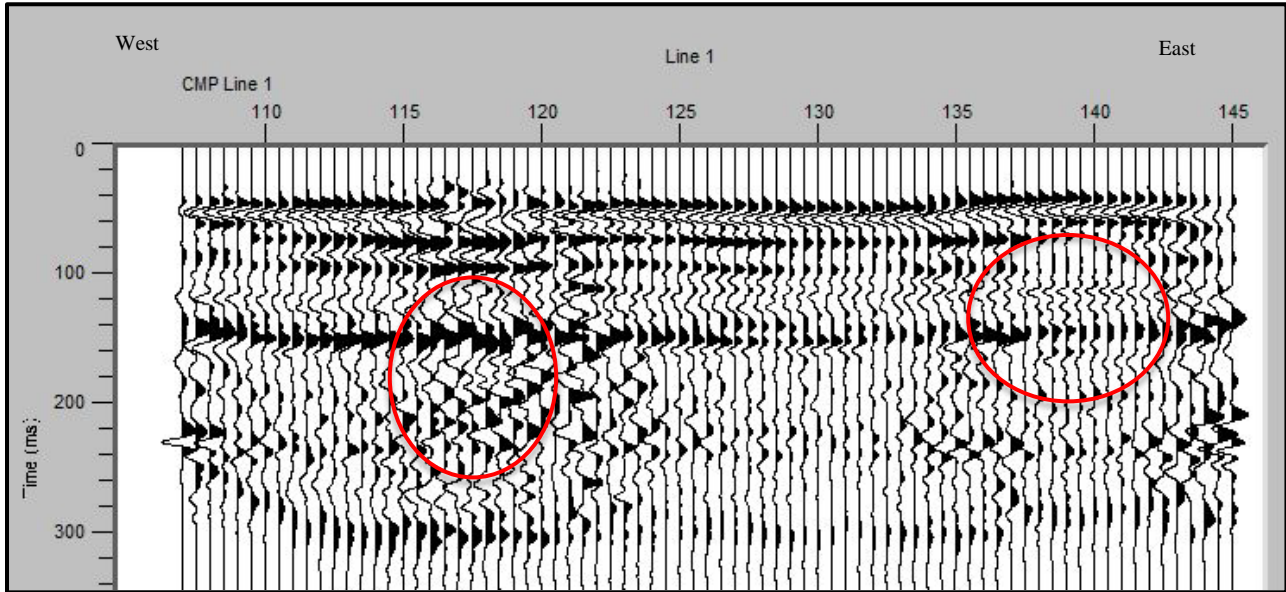


Figure 24: Seismic reflection line 1, with signal disruptions at CMP locations 117-121 and 137-141 (shown in red circles).

The increased amounts of noise present during the collection of line 2 are apparent in quality of reflections present (Figure 25). However, two clear reflections are visible in the data at approximately 40 ms and 100 ms, with a third discontinuous at approximately 60 ms. The reflections are disrupted at station locations 117-120, in the area on strike with a sand blow seen on the surface.

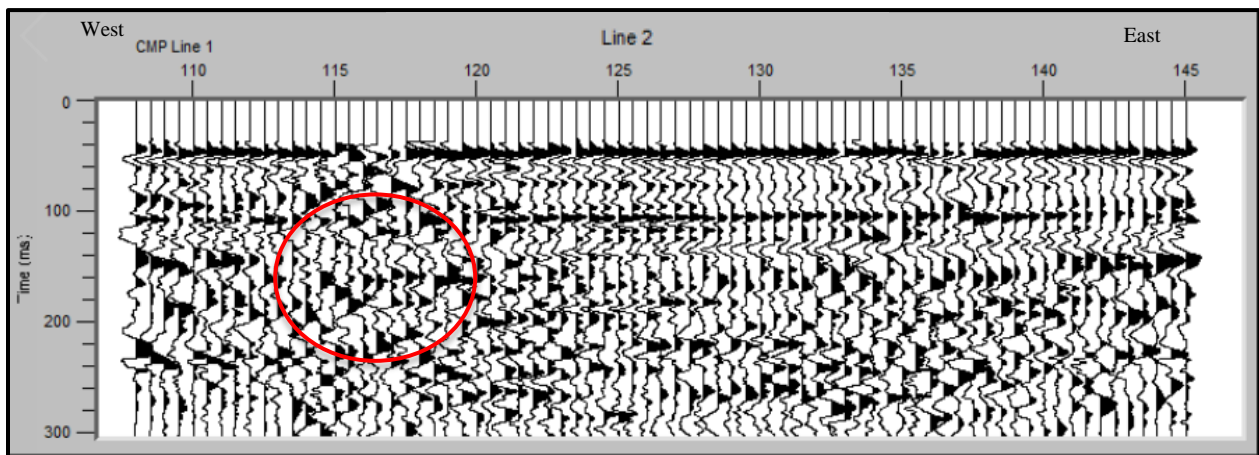


Figure 25: Seismic reflection line 2, with disrupted reflections between CMP locations 113-119 (shown in red circle).

Discussion

Areas of disrupted and offset reflections in both seismic lines are consistent with trends and locations of sand blows seen at the surface and interpreted from the electrical resistivity surveys and trench logs (Figures 26, 27, and 28). Taken together, these independent data sets are consistent with regional fault geometries (Figures 4 and 5). Figures 4 and 5 show the spatial proximity of the northeast-striking Eastern Rift Margin faults to the Pritchett site, suggesting that movement along this fault system could be the source of earthquakes related to the liquefaction features observed at the site and for the deformation seen in the seismic reflection lines.

The sand blows observed at the Pritchett site have two distinct directional trends, one set oriented north-south and the others northeast to southwest (Figure 28). This raises the probability that these two sets of blows may have originated from separate seismic events or sources. Other possible nearby sources for earthquakes are the northwest striking Reelfoot fault, and the northeast striking axial fault (Figure 5).

The prominent reflections in the seismic sections likely correlate with sediments of the Loess Upland Complex and Cockfield Formation. The vertical offset of the reflections (east side up) seen in the eastern part of seismic line 1 is likely related to the presence of the feeder dike and associated sand blow. Because the offset diminishes with depth and reflections suggest a more subtle downwarping of the strata, this deformation may be related to down-dropping from lateral spreading towards the riverbank located 0.25 km west of the profile (Figure 6). Some of the near-surface deformation is also likely due to the upward venting of liquified sediments from the source sand. The lack of deformation or offset of the deeper reflections observed in the data implies that the deformation affects only the near-surface strata. Thus, there is no convincing evidence of a subsurface fault located directly beneath the site.

Although no trench excavations were conducted along seismic line 2, the pattern and style of disrupted reflections seen in the data are similar to that seen in seismic line 1. The position of the profile also intersects a group of northeast-striking sand blows. As observed in seismic line 1, a slight offset up to the east of shallow reflections in the eastern part of the profile is observed. This offset is possibly related to deformation caused by a feeder dike connected to the observed sand blows.

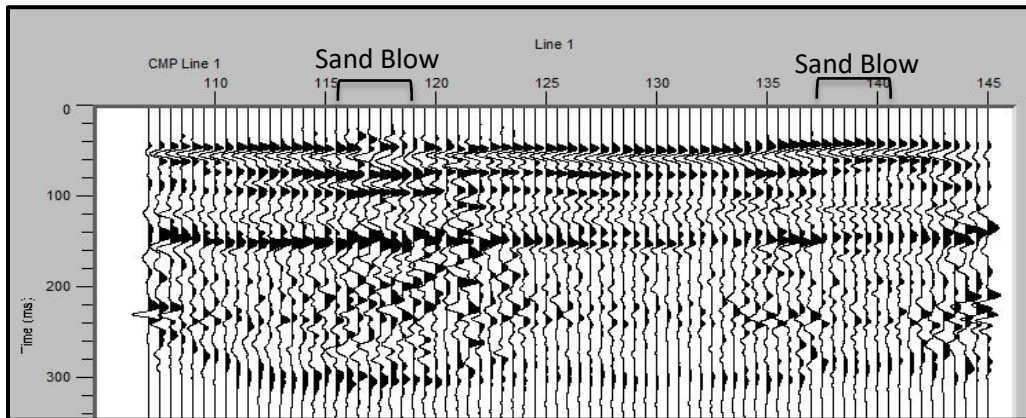


Figure 26: Seismic reflection line 1 with locations of sand blow deposits at surface labeled. Note disrupted reflections between locations roughly 116-119 and 137-141.

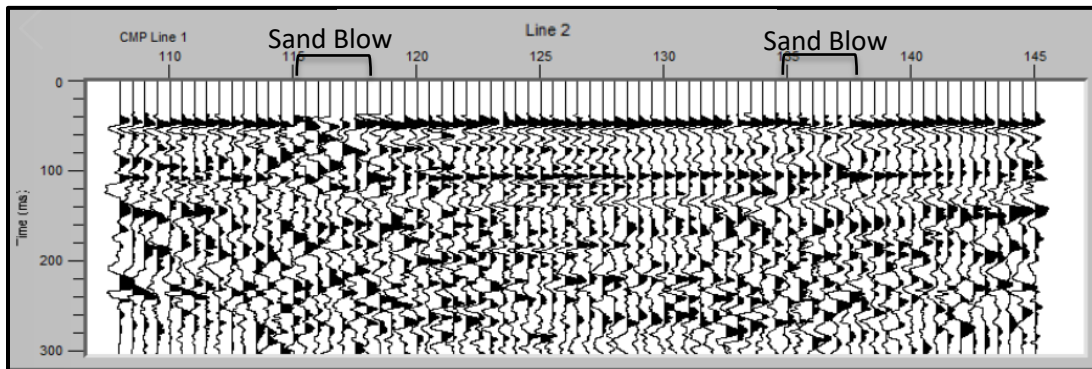


Figure 27: Seismic reflection line 2 with locations of sand blow deposits at surface labeled. Note disrupted reflections between locations roughly 115-118 and 135-138.



Figure 28: Pritchett site map showing location of seismic reflection surveys (red lines), with blue dots indicating positions of disrupted reflections on profiles (Figures 26 and 27) overlain on sand blows. Note two different orientations of sand blow deposits (see Discussion). Also shown are locations of electrical resistivity surveys (green lines) and trenches (yellow lines).

Conclusions

Discontinuous reflections seen in the seismic reflection data collected at the Pritchett site in western Tennessee provide subsurface information to ~90 m depth in an area of prominent northeast-trending sand blows. Disruptions in individual reflections are collocated with sand dikes observed in trench excavations and inferred from electrical resistivity surveys. Although the data provide evidence of near-surface deformation, the deformation appears to effect only shallow layers (< 13 m). Although the presence of an active fault in the vicinity is likely the source for the observed liquefaction features and near-surface deformation, there is no evidence in the seismic data that a fault is located at the Pritchett site beneath the seismic profiles. Rather,

the deformation observed is consistent with the formation of dikes in the liquefaction process and the possible cause of lateral spreading of upper layers toward the riverbank.

The results from the seismic reflection surveys in addition to the previous work and satellite images show a strong correlation in sand dike and sand blow orientations with the strike of regional faults. The proximity of the Eastern Margin Rift faults to the study area suggests that earthquakes originating from these faults may be the source of the liquefaction deposits. This, in addition to the microseismic activity in the area, raises the possibility that this fault system is currently active and in need of further research. Investigations of nearby liquefaction features, including gathering age ranges, would help to identify if the Eastern Margin Rift faults are the source of the features.

References

- Burger, H. R. (2006). Introduction to Applied Geophysics: Exploring the Shallow Subsurface, W.W. Norton. 200-205.
- Burke, K., and J. F. Dewey. (1973). Plume-generated triple junctions—Key indicators in applying tectonics to old rocks, *Geology*, **81**, 406-433.
- Csontos, R., & Van Arsdale, R. (2008). New Madrid seismic zone fault geometry, *Geosphere*, **4**, 802.
- Hardesty, K. (2008). Using Microtremors to Assess Site Characteristics in the New Madrid Seismic Zone [M.S. Thesis]: Auburn University, Auburn, Alabama, 88 p.
- Hildenbrand, T. G. (1985). Rift structure of the northern Mississippi embayment from the analysis of gravity and magnetic data, *Journal of Geophysical Research*, **90**, 12607–12622.
- Howe, James R., and Thomas L. Thompson. (1984). Tectonics, sedimentation, and hydrocarbon potential of the Reelfoot rift, *Journal of Geophysical Research*, **179**, 142-149.
- Liu, L., & Li, Y. (2001). Identification of liquefaction and deformation features using ground penetrating radar in the New Madrid seismic zone, USA, *Journal of Applied Geophysics*, **47**, 199–215.
- Luzietti, E. A., Kanter, & K. M. Shedlock (1992). Shallow deformation along the Crittenden County fault zone near the southeastern boundary of the Reelfoot Rift, northeast Arkansas, *Seismological Research Letters*, **63**, 263–275.
- Martin, J. (2014). Geophysical and geological analysis of fault activity and seismic history of the Obion river area, New Madrid Seismic Zone (NMSZ), western Tennessee, USA [M.S. Thesis]: Boston College, Boston, Massachusetts, 98 p.
- Martin, R. V., & Van Arsdale, R. B. (2017). Stratigraphy and structure of the Eocene Memphis Sand above the eastern margin of the Reelfoot Rift in Tennessee, Mississippi, and Arkansas, USA, *Geological Society of America Bulletin*, **31**, 345-356.
- Nelson, K. D., & Zhang, J. (1991). A COCORP deep reflection profile across the buried Reelfoot Rift, south-central United States, *Tectonophysics*, **197**, 271–293.
- Obermeier, S. F., & Dickenson, S. E. (2000). Liquefaction evidence for the strength of ground motions resulting from Late Holocene Cascadia subduction earthquakes, with emphasis on the event of 1700 A.D., *Bulletin of the Seismological Society of America*, **90**, 876–896.
- Saucier, R. T. (1991). Geoarchaeological evidence of strong prehistoric earthquakes in the New Madrid (Missouri) seismic zone, *Geology*, **19**, 296–298.

- Street, R., Woolery, E. W., & Chiu, J. M. (2004). Shear-wave velocities of the post-Paleozoic sediments across the Upper Mississippi Embayment, *Seismological Research Letters*, **75**, 390–405.
- Tuttle, M. P., Lafferty, R. H., Cande, R. F., & Sierzchula, M. C. (2011). Impact of earthquake-induced liquefaction and related ground failure on a Mississippian archeological site in the New Madrid seismic zone, central USA, *Quaternary International*, **242**, 126–137.
- Tuttle, M. P., Schweig, E. S., Sims, J. D., Lafferty, R. H., Wolf, L. W., & Haynes, M. L. (2002). The earthquake potential of the New Madrid seismic zone, *Bulletin of the Seismological Society of America*, **92**, 2080–2089.
- Van Arsdale, R. B. & TenBrink, R. K. (2000). Late Cretaceous and Cenozoic geology of the New Madrid seismic zone, *Bulletin of the Seismological Society of America*, **90**, 345–356.
- Wolf, L. W., M-K Lee, S. Browning, and M. Tuttle. (2005). Numerical analysis of overpressure development in the New Madrid seismic zone, *Bulletin of the Seismological Society of America*, **95**, 135-144.
- Woolery, E. W., Street, R. L., Wang, Z., Harris, J. B., & McIntyre, J. (1999). Neotectonic structure in the central New Madrid seismic zone: Evidence from multimode seismic reflection data, *Seismological Research Letters*, **70**, 554-576.

APPENDICES

Appendix A

Table 1: Observer Notes

Field File	Src. Line	Src. Location	First Channel	Last Channel	Channel Increment	Recv. Line	First Recv.	Recv. Incr.
6251	1	101	1	24	1	1	104	1
6252	1	102	2	25	1	1	105	1
6253	1	103	3	26	1	1	106	1
6254	1	104	4	27	1	1	107	1
6255	1	105	5	28	1	1	108	1
6256	1	106	6	29	1	1	109	1
6257	1	107	7	30	1	1	110	1
6258	1	108	8	31	1	1	111	1
6259	1	109	9	32	1	1	112	1
6260	1	110	10	33	1	1	113	1
6261	1	111	11	34	1	1	114	1
6262	1	112	12	35	1	1	115	1
6263	1	113	13	36	1	1	116	1
6264	1	114	14	37	1	1	117	1
6265	1	115	15	38	1	1	118	1
6266	1	116	16	39	1	1	119	1
6267	1	117	17	40	1	1	120	1
6268	1	118	18	41	1	1	121	1
6269	1	119	19	42	1	1	122	1
6270	1	120	20	43	1	1	123	1
6271	1	121	21	44	1	1	124	1
6272	1	122	22	45	1	1	125	1
6273	1	123	23	46	1	1	126	1
6274	1	124	24	47	1	1	127	1
6275	1	125	25	48	1	1	128	1
6276	1	126	26	48	1	1	129	1
6277	1	127	27	48	1	1	130	1
6278	1	129	28	48	1	1	131	1
6279	1	130	29	48	1	1	132	1
6280	1	131	30	48	1	1	133	1
6281	1	132	31	48	1	1	134	1
6282	1	133	32	48	1	1	135	1
6283	1	134	33	48	1	1	136	1
6284	1	135	34	48	1	1	137	1
6285	1	136	35	48	1	1	138	1
6286	1	137	36	48	1	1	139	1

6287	1	138	37	48	1	1	140	1
6288	1	139	38	48	1	1	141	1
6289	1	140	39	48	1	1	142	1
6290	1	141	40	48	1	1	143	1
6291	1	142	41	48	1	1	144	1
6292	1	143	42	48	1	1	145	1
6293	1	144	43	48	1	1	146	1
6294	1	145	44	48	1	1	147	1
6295	1	146	45	48	1	1	148	1
6296	1	147	46	48	1	1	149	1
6297	1	148	47	48	1	1	150	1
6298	1	149	48	48	1	1	151	1

Table 2: Source Location Notes

Source Line	Source Location	Easting	Northing	Elevation
1	101	0	0	0
1	102	3	0	0
1	103	6	0	0
1	104	9	0	0
1	105	12	0	0
1	106	15	0	0
1	107	18	0	0
1	108	21	0	0
1	109	24	0	0
1	110	27	0	0
1	111	30	0	0
1	112	33	0	0
1	113	36	0	0
1	114	39	0	0
1	115	42	0	0
1	116	45	0	0
1	117	48	0	0
1	118	51	0	0
1	119	54	0	0
1	120	57	0	0
1	121	60	0	0
1	122	63	0	0
1	123	66	0	0
1	124	69	0	0

1	125	72	0	0
1	126	75	0	0
1	127	78	0	0
1	128	81	0	0
1	129	84	0	0
1	130	87	0	0
1	131	90	0	0
1	132	93	0	0
1	133	96	0	0
1	134	99	0	0
1	135	102	0	0
1	136	105	0	0
1	137	108	0	0
1	138	111	0	0
1	139	114	0	0
1	140	117	0	0
1	141	120	0	0
1	142	123	0	0
1	143	126	0	0
1	144	129	0	0
1	145	132	0	0
1	146	135	0	0
1	147	138	0	0
1	148	141	0	0

Table 3: Receiver Location Notes

Receiver Line	Receiver Location	Easting	Northing	Elevation
1	104	9	0	0
1	105	12	0	0
1	106	15	0	0
1	107	18	0	0
1	108	21	0	0
1	109	24	0	0
1	110	27	0	0
1	111	30	0	0
1	112	33	0	0
1	113	36	0	0
1	114	39	0	0
1	115	42	0	0

1	116	45	0	0
1	117	48	0	0
1	118	51	0	0
1	119	54	0	0
1	120	57	0	0
1	121	60	0	0
1	122	63	0	0
1	123	66	0	0
1	124	69	0	0
1	125	72	0	0
1	126	75	0	0
1	127	78	0	0
1	128	81	0	0
1	129	84	0	0
1	130	87	0	0
1	131	90	0	0
1	132	93	0	0
1	133	96	0	0
1	134	99	0	0
1	135	102	0	0
1	136	105	0	0
1	137	108	0	0
1	138	111	0	0
1	139	114	0	0
1	140	117	0	0
1	141	120	0	0
1	142	123	0	0
1	143	126	0	0
1	144	129	0	0
1	145	132	0	0
1	146	135	0	0
1	147	138	0	0
1	148	141	0	0
1	149	144	0	0
1	150	147	0	0
1	151	150	0	0

Appendix B

Data collected for this study is available as an electronic supplement through the AUrora:
Auburn University Scholarly Repository. <http://hdl.handle.net/11200/49352>